Chinese Chemical Letters 32 (2021) 2909–2913

Contents lists available at ScienceDirect

Chinese Chemical Letters

journal homepage: www.elsevier.com/locate/cclet

Communication

Solvent regulation strategy of Co-MOF-74 microflower for supercapacitors

Changli Wang[a], Xinran Li[a], Wenping Yang[a], Yuxia Xu[b,*], Huan Pang[a,*]

[a] School of Chemistry and Chemical Engineering, Yangzhou University, Yangzhou 225009, China
[b] Guangling College, Yangzhou University, Yangzhou 225009, China

ARTICLE INFO

Article history:
Received 30 December 2020
Revised 6 April 2021
Accepted 9 April 2021
Available online 16 April 2021

Keywords:
Metal-organic frameworks
Solvent regulation strategy
Co-MOF-74 microflower
Pseudocapacitive-controlled behavior
Asymmetric supercapacitor device

ABSTRACT

Metal-organic frameworks (MOFs) with porous crystal structures have attracted extensive attention in application of energy storage and conversion, owing to their regularity, porosity, large specific surface area, *etc*. In this work, Co-MOF-74 microflower has been successfully prepared *via* a controllable solvent regulation strategy. Through modulating the polarity of the solvent, crystals grow in certain preferred orientation and Co-MOF-74 with various morphologies were obtained. Thereinto, the energy storage performance of Co-MOF-74 microflower was measured in both three-electrode system and asymmetric supercapacitor device (specific capacitance of 164.2 F/g at 0.5 A/g in the three-electrode system and 62.5 F/g at 1 A/g in the asymmetric supercapacitor device). This can be attributed to the preferred crystal orientation resulting in a regular and uniform microflower, which is of great significance to electronic interfacial exchange and ion transfer during electrochemical reactions.

The increasing energy dilemma and environmental contamination have called for the rapid development of clean energy sources as well as excellent devices for energy storage and conversion [1,2]. Supercapacitors (SCs), serving as a potential energy storage device, possess plenty of advantages, *e.g.*, high charge-discharge rate, large specific power, and long cycling life [3,4]. There are typically two broad categories of SCs based on different functional mechanisms of charge storage, including pseudocapacitors and electric double layer capacitors (EDLCs) [5]. Pseudocapacitors store charge mainly through fast and reversible faradaic reactions while EDLCs store energy *via* accumulating charge at the surface of electrode or at the boundary of the electrolyte. In the last few decades, carbon-based materials [6,7], metal oxides [8,9], and conductive polymers [10,11] have been continuously investigated as conventional electrode materials for SCs. However, the inherent deficiency of these materials (unsatisfied performance of commercial activated carbon [12]; high price and pollution of metal oxides [13,14]; poor thermal stability and cycling performance of conductive polymers [15]) limit the practical applications for SCs to some extent [16–18]. Hence, researches have been conducted on the synthesis of electrode materials which can be attributed to two points to enhance the energy storage performance: (1) Design materials with large specific area and porosity to facilitate electronic interfacial exchange and ion transfer [19]; (2) Build ordered and stable microstructure to enhance cycling stability [20].

Recently, metal-organic frameworks (MOFs) with porous crystal structures have attracted extensive attention due to its regularity, porosity, large specific surface area, which are beneficial to improve the electron and ion transfer during electrochemical reactions [21–24]. In addition, the outer electron orbits of the metal cations, especially transition metal, within MOFs have multiple electron arrangements, which can produce multi-level redox behaviors and provide more opportunities for charge storage [25–29]. More importantly, through controllably synthetic strategies, the structure, composition and morphology of MOFs can be precisely regulated, which are crucial factors to the energy storage performance of electrode materials [30–33].

Co-MOF-74, commonly with a hexagonal rod structure, is well-known for its stable structure, high surface area due to the adjustable metal nodes and oxygen-rich dicarboxylic acid ligand [34–37]. In this work, we have prepared Co-MOF-74 microflower through a facile one-pot solvothermal procedure. Moreover, the relationship of solvent polarity and crystal growth are investigated to controllably synthesize Co-MOF-74 with various morphologies. The regular and uniform microflower aggregate of Co-MOF-74 accelerates the interfacial electron and ion transfer and enhances the electrochemical stability. When utilized as the electrode material for SCs, the Co-MOF-74 microflower exhibits a satisfied charge stor-

* Corresponding authors.
E-mail addresses: xuyuxia1105@163.com (Y. Xu), panghuan@yzu.edu.cn (H. Pang).

https://doi.org/10.1016/j.cclet.2021.04.017
1001-8417/

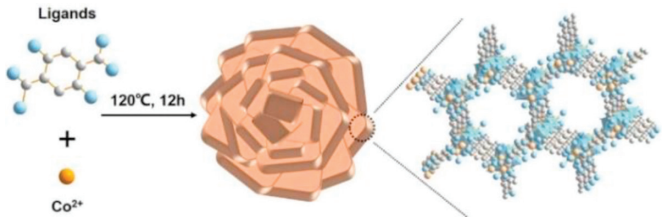

Scheme 1. Abridged general view of the synthetic process of Co-MOF-74.

age performance in both three-electrode system and asymmetric supercapacitor device. The solvent regulation strategy for MOF fabrication in this work is facile and efficient, indicating a promising application prospect for the preparation of MOF-based electrode materials in the field of electrochemical energy storage and conversion.

Scheme 1 clearly illustrates the one-pot synthetic procedure of Co-MOF-74 microflower, all the samples are obtained at a 120 °C solvothermal treatment for 12 h. Firstly, in methanol solution, the morphology of the as-prepared Co-MOF-74 is exhibited in the scanning electron microscopy (SEM) images of Figs. S1a and b (Supporting information). The resulting granules are highly stacked into amorphous piles. When absolute ethanol is utilized as solvent, the obtained sample presents a two-dimensional rod structure (Figs. S1c and d in Supporting information) with an uneven shape and size. Subsequently, modulating the solvent polarity by the ethanol and deionized water (2:1, v/v), crystals grow in certain preferred orientation resulting in a novel and uniform microflower structure (Figs. S1e and f in Supporting information). From the above results, it can be speculated that the morphology of Co-MOF-74 is greatly affected by the solvent polarity. This is ascribed to the different polarity environments that influence the crystal orientation of Co-MOF-74, forming various aggregates.

Powder X-ray diffraction (PXRD) is carried out to investigate the crystal structure of the as-prepared Co-MOF-74 microflower, as shown in Fig. 1a. According to the results, the diffraction peaks occurring at $2\theta = 6.7°$ and 11.6° are corresponded to (2 $\bar{1}$ 0) and (3 0 0), respectively (CCDC No. 1494752), which is consistent with the simulated XRD pattern of Co-MOF-74 [38]. Here, the solvent plays a critical role in the preparation of MOFs, influencing the self-assembly process between metallic ions and organic ligand. Moreover, it is utilized as a structural inductive agent or a crystal media to direct the crystal orientated growth, inducing in the formation of (2 $\bar{1}$ 0) and (3 0 0) planes in this work. In addition, for the purpose of better identification of the valence state of the obtained samples, X-ray photoelectron spectroscopy (XPS) is performed to analyze the Co-MOF-74 microflower. The XPS survey spectrum from Fig. 1b shows that the tested sample consists of C, O and Co elements, and the result is consistent with energy dispersion X-ray analysis (EDX**,** depicted in Fig. S2 in Supporting information) as well [39,40]. The Co 2p spectrum in Fig. 1c presents two major peaks at 797.8 eV–781.5 eV along with a spin energy separation of ~16 eV, corresponding to the Co $2p_{1/2}$ and Co $2p_{3/2}$ state, respectively. The other two broad peaks located at around 785.9 –802.7 eV are identified as satellites peaks (noted as "Sat.") [41,42]. Additionally, the C 1s spectrum in Fig. 1d is divided into three peaks at 284.7, 286.1 and 288.1 eV, which can be associated with C–C, C–O and C=O, respectively [43]. These results confirmed that the crystal structure and valence state of the obtained Co-MOF-74 microflower are consistent with the well-known Co-MOF-74 [44,45].

SEM is utilized to observe the morphology of the as-prepared samples. SEM image in Fig. 2a clearly demonstrates that the Co-MOF-74 microflower with a uniform and regular size is well dispersed and the average diameter is approximately 2–3 μm. Through SEM images with higher resolution in Fig. 2b, it can be observed that the Co-MOF-74 microflower is orderly assembled from nanoplates, and that the hierarchical structure enlarges the contact with electrolyte and benefits ion and electron transfer. The transmission electron microscopy (TEM) of Co-MOF-74 microflower in Fig. 2c is consistent with the SEM images, the solid hierarchical structure with no obvious external defects avoiding the aggregation and collapse of microstructure during the electrochemical reactions. Furthermore, the presence of C, O and Co elements is confirmed by EDX detection and elemental mapping images in Figs. 2d-g, and all the elements were evenly distributed throughout the Co-MOF-74 microflower.

The pseudocapacitive performance of the Co-MOF-74 microflower-based working electrode is tested in 3 mol/L KOH *via* cyclic voltammetry (CV) technology in a three-electrode system. The CV curves of Co-MOF-74 microflower-based working electrode at a scan rate from 5 mV/s to 100 mV/s with a loading mass of ~1.5 mg/cm^2 are exhibited in Fig. 3a. The shapes of CV curves are typically pseudocapactive behavior in the potential window from 0 V to 0.5 V (*vs.* Hg/HgO) with corresponding catholic peak (~0.23 V) and anodic peak (~0.34 V) [46]. These Faradaic features are possibly due to the redox reactions of Co^{2+}/Co^{3+} under the action of OH^- during the electrochemical reactions [47]. To investigate the capacitive behavior of the Co-MOF-74 microflower, galvanostatic charge-discharge (GCD) measurement is employed in a three-electrode system. The resulting GCD curves of the Co-MOF-74 microflower are depicted in Fig. 3b. It can be observed that the Co-MOF-74 microflower-based working electrode exhibits symmetrical charge and discharge curves in the entire current density range, which corresponds to the excellent reversible redox reaction [48,49]. Specific capacitances of 164.2, 153.2, 148.8, 145.8, 136.0 and 122.0 F/g are achieved by Co-MOF-74 microflower-based working electrode at a current density of 0.5, 1.0, 2.0, 3.0, 5.0 and 10.0 A/g, respectively with the Coulomb efficiency reaching up to 83% (details of calculation are shown in Supporting information). Concluded from the specific capacitance performances of the working electrode in Fig. 3c, with the increase of current density, the specific capacitance declined from 164.2 F/g to 122.0 F/g, which resulted from ionic insufficient contact with the holes inside the electrode materials at high current densities. Fig. 3d exhibits the capacitance retention of the Co-MOF-74 microflower-based working electrode. More than 75% of the initial capacitance was maintained at 10 A/g after 1500 charge-discharge cycles. Here, taking into account of the previous reports, the comparison of energy storage performance between the as-prepared Co-MOF-74 microflower and other similar electrode materials is concluded in Table S1 (Supporting information). Moreover, electrochemical impedance spectroscopy (EIS) measurements (organized into Nyquist plot) are conducted on the Co-MOF-74 microflower at an open circuit potential, as exhibited in Fig. S3 (Supporting information). The nearly linear EIS plot in the low-frequency region is the typically feature of Warburg impedance, representing the electrolyte diffusion within samples [50]. And a relatively high slope of the EIS plot implies a fluent electrolyte diffusion on the surface of samples owing to suitable pore size.

To gain insights into the total charge storage mechanism, the pseudocapacitive kinetics is estimated *via* analyzing CV curves at various scan rates based on the relationship between peak current (i) and the scan rate (v). As exhibited in Eqs. 1 and 2, a and b are regulating parameters. If $b = 0.5$, it is indicated that the electrochemical process is diffusion-controlled. If $b = 1$, the electrochemical process is a pseudocapacitive-controlled behavior. When $0.5 < b < 1$, the electrochemical kinetics contains both the diffusion-controlled and pseudocapacitive-controlled process. Taking into account the relationship between $\log(i)$ and $\log(v)$

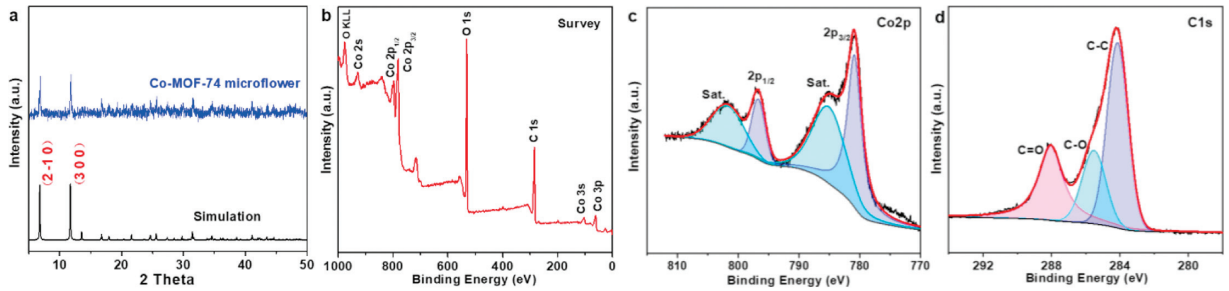

Fig. 1. (a) XRD pattern and (b-d) XPS spectra of Co-MOF-74 microflower: (b) Survey, (c) Co 2p, (d) C 1s. The red curves in (c) and (d) are the fitting curves and the black curves are the test data.

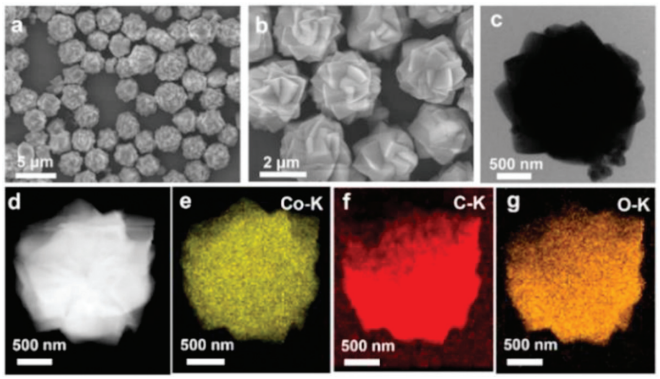

Fig. 2. (a, b) SEM images, (c) TEM image, (d) STEM image and (e-g) corresponding mapping images of Co-MOF-74 microflower.

(Fig. 3e), the b value of the oxidation peak and reduction peak for Co-MOF-74 microflower is 0.85 and 0.71, respectively, indicating that the electrochemical kinetics are mainly ascribed to the pseudocapacitive-controlled behavior. Furthermore, the contributions of pseudocapacitive/diffusion-controlled process are analyzed according to the Eq. 3 at different scan rates. Thereinto, k_1v and $k_2v^{1/2}$ have the close connection with the surface pseudocapacitive effect and the diffusion-controlled process, respectively. Fig. S4 (Supporting information) depicts that the ratio of pseudocapacitive contribution of the Co-MOF-74 microflower is 53.89%, 58.73%, 65.72%, 70.31%, 78.58% and 94.70% at a scan rate of 5, 10, 20, 30, 50, 100 mV/s, respectively. Correspondingly, the contribution ratio of pseudocapacitive *vs.* diffusion at different scan rates are listed in Fig. 3f. Owing to the limited ionic intercalation into lattices, the diffusion-controlled contribution gradually decreases with the increase of the scan rate, which is consistent with the obtained results. Analyzed from the electrochemical kinetic properties, the high ratio of pseudocapacitive contribution can be attributed to its large specific surface area, good conductivity, and fast ion diffusion channels of the unique miccroflower structure, which is beneficial to energy storage performance.

$$i = av^b \tag{1}$$

$$\log(i) = b\log(v) + \log(a) \tag{2}$$

$$i(\mathrm{V}) = k_1v + k_2v^{1/2} \tag{3}$$

In addition, to comprehend the microstructural change of samples after the electrochemical test, SEM and TEM analysis are conducted for the Co-MOF-74 microflower following the electrochemical test. The corresponding post-test SEM and TEM images are exhibited in Fig. S5 (Supporting information), implying that the whole microflower structure is well maintained. However, the

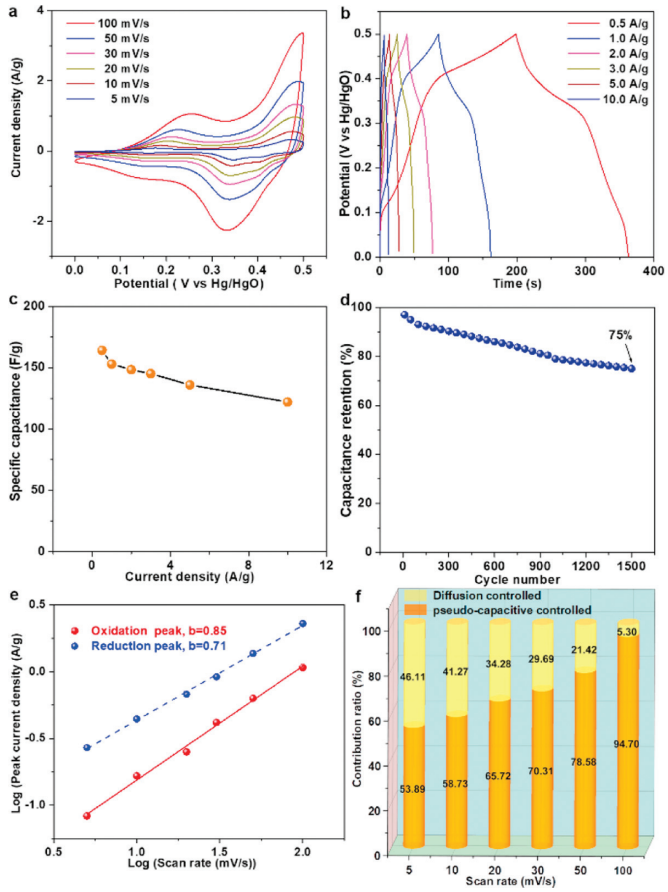

Fig. 3. Electrochemical performances of Co-MOF-74 mircoflower-based working electrode in a three-electrode system. (a) CV curves at different scan rates. (b) GCD curves at different current densities. (c) Specific capacitance performances at a current density from 1 A/g to 10 A/g. (d) Capacitance retention at a current density of 10 A/g. (e) Relationship between log(i) and log(v) of Co-MOF-74 microflower. (f) Contribution ratio of pseudocapacitive *vs.* diffusion at different scan rates.

slight aggregation of Co-MOF-74 microflower with the size increasing from ~3 μm to ~4 μm and the decline of the surface regularity result in the encapsulation of partial active sites and the decrease its specific surface area. And, the crack in the center of Co-MOF-74 microflower causes a hole in the middle of the TEM image, which may bring about the electrochemical performance degradation. In addition, the XRD pattern of the Co-MOF-74 microflower-based Ni foam after the electrochemical test is exhibited in Fig. S6 (Supporting information). The XRD result manifests that there is no obvious formation of other peaks in the composition of the Co-MOF-74 microflower-based Ni foam. However, the former distinct peaks at $2\theta = 6.7°$ and 11.6° have been converted to a bulge at $2\theta = 5°–15°$,

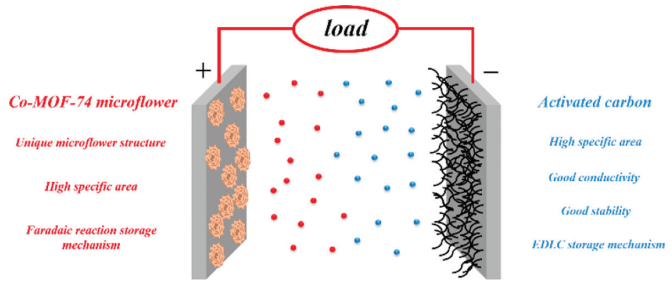

Fig. 4. An abstract illustration of asymmetric supercapacitor device using Co-MOF-74 microflower and AC as a positive and negative material, respectively.

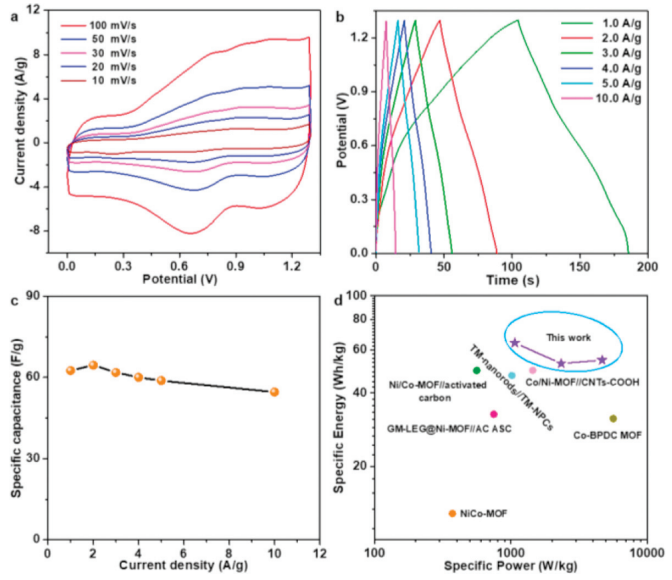

Fig. 5. (a) CV curves at different scan rates. (b) GCD curves at different current densities. (c) Specific capacitance performances varied from current densities. (d) Comparison of electrochemical performances tested in Co-MOF-74 microflower//AC with different reported electrode materials over ragone plots (specific energy *vs.* specific power).

indicating the damage to the crystal structure of Co-MOF-74 microflower to some extent during the electrochemical test.

To further assess the potential application of Co-MOF-74 microflower, an asymmetric supercapacitor device using Co-MOF-74 microflower as the positive material and commercial activated carbon (AC) as the negative material was assembled (denoted as Co-MOF-74 microflower//AC), as shown in Fig. 4. Co-MOF-74 microflower with a unique microstructure can provide enough space for OH^- intercalation and deintercalation (pseudocapacitors). Meanwhile, AC plays a key role in providing fast surface reactions as well as charge transfer (EDLCs). Therefore, the as-assembled asymmetric supercapacitor device possesses the advantages of both pseudocapacitors and EDLCs to improve specific energy and specific power simultaneously.

In the CV curves of Fig. 5a, the Co-MOF-74 microflower//AC exhibits a mixed behavior of pseudocapacitors and EDLCs with the voltage window of 0–1.3 V at different scan rates, which cover an extra-large current area compared with the pristine three-electrode system. In Fig. 5b, the Co-MOF-74 microflower//AC exhibits the symmetrical charge and discharge curves with Coulomb efficiency reaching to 78% [51]. The values of specific capacitances at 1, 2, 3, 4, 5 and 10 A/g calculated from the GCD curves are 62.5, 64.5, 61.8, 60, 58.8 and 54.6 F/g, respectively, as shown in Fig. 5c. And the corresponding cycling capacitance is carried out in Fig. S7 (Supporting information). Though the capacitance exhibits a gradual drop with the increase of cycle numbers, it still maintains 70% of its initial capacitance at a high current density of 10 A/g, showing great long-term cycling stability. Moreover, specific energy and specific power were organized into Ragone plot in comparison with some reported MOFs-based SCs, as exhibited in Fig. 5d. The detail calculations of the specific power (*P*, W/kg) and specific energy (*E*, Wh/kg) are given in Supporting information. It can be obviously observed that the Co-MOF-74 microflower//AC performs well compared to the similar materials. In order to further investigate the electrochemical performance of the Co-MOF-74 microflower//AC, CV and GCD with different voltage ranges are conducted, as shown in Figs. S8 and S9 (Supporting information). And specific energies of 64.1, 52.8–54.5 Wh/kg and corresponding specific powers of 1080, 2340–4683 W/kg are plotted in Fig. S10 (Supporting information).

EIS measurement is also applied in the Co-MOF-74 microflower//AC, and the Nyquist plot is presented in Fig. S11 (Supporting information). The small charge transfer resistance during the experiment can be observed from the semicircle shape in the first part of the curve, and the good conductivity can be acquired through the high slope of the vertical line in the second part of the curve. In general, thanks to the participation of AC, the overall conductivity and the stability of the device are both significantly improved, rendering Co-MOF-74 very suitable for asymmetric supercapacitor devices.

In summary, through the investigation of the relationship between the microstructure and solvent polarity, a series of Co-MOF-74 with various morphologies has been synthesized *via* the solvent regulation strategy. The as-prepared Co-MOF-74 microflower exhibits the satisfied energy storage performance (specific capacitance of 164.2 F/g at 0.5 A/g in the three-electrode system and 62.5 F/g at 1 A/g in the asymmetric supercapacitor device). This can be ascribed to the regular and uniform microflower aggregates that ensure the thorough exposure of materials in the electrolyte and provide more pathways and sites for electronic interfacial exchange and ion transfer, benefiting to the reversible redox kinetics and enhancing the electrochemical performance. The corresponding analytic details of kinetics characteristic for Co-MOF-74 microflower is given in this work. Furthermore, the solvent regulation strategy for MOF fabrication in this work is facile and efficient, indicating a promising application prospect for the preparation of MOF-based electrode materials in the field of electrochemical energy storage and conversion.

Declaration of competing interest

The authors declare that they have no known competing financial interests or personal relationships that could have appeared to influence the work reported in this paper.

Acknowledgments

This work was supported by the National Natural Science Foundation of China (Nos. U1904215, 21671170, 21673203), the Top-notch Academic Programs Project of Jiangsu Higher Education Institutions (TAPP), Changjiang scholars program of the Ministry of Education (No. Q2018270), Excellent doctoral dissertation of Yangzhou university and Undergraduate scientific research innovation projects in Jiangsu province (No. 201911117036Z).

Supplementary materials

Supplementary material associated with this article can be found, in the online version, at doi:10.1016/j.cclet.2021.04.017.

References

[1] S. Zheng, X. Li, B. Yan, et al., Adv. Energy Mater. 7 (2017) 1602733.
[2] X. Xiao, L. Zou, H. Pang, Q. Xu, Chem. Soc. Rev. 49 (2020) 301–331.
[3] F.B. Ajdari, E. Kowsari, M.N. Shahrak, et al., Coord. Chem. Rev. 422 (2020) 213441.
[4] M. Du, Q. Li, Y. Zhao, C.S. Liu, H. Pang, Coord. Chem. Rev. 416 (2020) 213341.
[5] A. Muzaffar, M.B. Ahamed, K. Deshmukh, J. Thirumalai, Renew. Sustain. Energy Rev. 101 (2019) 123–145.
[6] K. Jayaramulu, D.P. Dubal, B. Nagar, et al., Adv. Mater. 30 (2018) 1705789.
[7] L. Miao, D. Zhu, M. Liu, et al., Chem. Eng. J. 347 (2018) 233–242.
[8] W. Guo, C. Yu, S. Li, et al., Adv. Mater. 31 (2019) 1901241.
[9] B.Y. Guan, A. Kushima, L. Yu, et al., Adv. Mater. 29 (2017) 1605902.
[10] P. Li, Z. Jin, L. Peng, et al., Adv. Mater. 30 (2018) 1800124.
[11] W. Zhang, P. Feng, J. Chen, Z. Sun, B. Zhao, Prog. Polym. Sci. 88 (2019) 220–240.
[12] Z. Bi, Q. Kong, Y. Cao, et al., J. Mater. Chem. A 7 (2019) 16028–16045.
[13] C. Qu, B. Zhao, Y. Jiao, et al., ACS Energy Lett. 2 (2017) 1263–1269.
[14] C. Qu, L. Zhang, W. Meng, et al., J. Mater. Chem. A 6 (2018) 4003–4012.
[15] J. Han, H. Wang, Y. Yue, et al., Carbon N. Y. 149 (2019) 1–18.
[16] B. Zhu, Z. Liang, D. Xia, R. Zou, Energy Storage Mater. 23 (2019) 757–771.
[17] R. Zhao, Z. Liang, R. Zou, Q. Xu, Joule 2 (2018) 2235–2259.
[18] X. Liu, W. Zang, C. Guan, et al., ACS Energy Lett. 3 (2018) 2462–2469.
[19] J. Zhao, H. Li, C. Li, et al., Nano Energy 45 (2018) 420–431.
[20] X. Li, X. Yang, H. Xue, H. Pang, Q. Xu, EnergyChem 2 (2020) 100027.
[21] L. Zou, C.C. Hou, Z. Liu, H. Pang, Q. Xu, J. Am. Chem. Soc. 140 (2018) 15393–15401.
[22] B. Liu, H. Shioyama, H. Jiang, X. Zhang, Q. Xu, Carbon 48 (2010) 456–463.
[23] X. Cao, C. Tan, M. Sindoro, H. Zhang, Chem. Soc. Rev. 46 (2017) 2660–2677.
[24] M. Du, M. Chen, X.G. Yang, et al., J. Mater. Chem. A 2 (2014) 9828–9834.
[25] S. Zhang, Z. Yang, K. Gong, et al., Nanoscale 11 (2019) 9598–9607.
[26] L. Wang, P. Tang, J. Liu, et al., J. Colloid Interface Sci. 554 (2019) 260–268.
[27] C. Young, J. Kim, Y.V. Kaneti, Y. Yamauchi, ACS Appl. Energy Mater. 1 (2018) 2007–2015.
[28] J. Xing, K. Guo, Z. Zou, et al., Chem. Commun. 54 (2018) 7046–7049.
[29] S. Zhou, S. Wang, S. Zhou, et al., Nanoscale 12 (2020) 8934–8941.
[30] Y. Li, Y. Xu, Y. Liu, H. Pang, Small 15 (2019) 1902463.
[31] X. Guo, Y. Xu, Y. Cheng, Y. Zhang, H. Pang, Appl. Mater. Today 18 (2020) 100517.
[32] Y. Jiao, J. Pei, D. Chen, et al., J. Mater. Chem. A 5 (2017) 1094–1102.
[33] H. Xia, J. Zhang, Z. Yang, et al., Nano-Micro Lett. 9 (2017) 43.
[34] X. Zhang, C.Y. Chuah, P. Dong, et al., ACS Appl. Mater. Interfaces 10 (2018) 43316–43322.
[35] C. Yu, Y. Wang, J. Cui, et al., J. Mater. Chem. A 6 (2018) 8396–8404.
[36] G. Zhu, H. Wen, M. Ma, et al., Chem. Commun. 54 (2018) 10499–10502.
[37] C. Ren, X. Jia, W. Zhang, et al., Adv. Funct. Mater. (2020) 2004519.
[38] W. Wong-Ng, J.A. Kaduk, H. Wu, M. Suchomel, Powder Diffr. 27 (2012) 256–262.
[39] Q. Wu, R. Xu, R. Zhao, et al., Energy Storage Mater. 19 (2019) 69–79.
[40] J. Yu, X. Gao, Z. Cui, et al., Energy Technol. 7 (2019) 1900018.
[41] S. Chen, M. Xue, Y. Li, et al., J. Mater. Chem. A 3 (2015) 20145–20152.
[42] P.C. Banerjee, D.E. Lobo, R. Middag, et al., ACS Appl. Mater. Interfaces 7 (2015) 3655–3664.
[43] T. Deng, Y. Lu, W. Zhang, et al., Adv. Energy Mater. 8 (2018) 1702294.
[44] Q. Yang, Z. Li, R. Zhang, et al., Nano Energy 41 (2017) 408–416.
[45] B. Li, P. Gu, Y. Feng, et al., Adv. Funct. Mater. 27 (2017) 1605784.
[46] S. Zheng, X. Guo, H. Xue, et al., Chem. Commun. 55 (2019) 10904–10907.
[47] D. Sun, Y. Tang, D. Ye, et al., ACS Appl. Mater. Interfaces 9 (2017) 5254–5262.
[48] C. Guan, W. Zhao, Y. Hu, et al., Nanoscale Horiz. 2 (2017) 99–105.
[49] H. Zhang, B. Xu, H. Mei, et al., Small 15 (2019) 1904663.
[50] A. Jayakumar, R.P. Antony, R. Wang, J.M. Lee, Small 13 (2017) 1603102.
[51] G.J.H. Lim, X. Liu, C. Guan, J. Wang, Electrochim. Acta 291 (2018) 177–187.